Magnetic interlayer exchange coupling in epitaxial Fe/Si/Fe(001) studied by polarized neutron reflectometry

R. W. E. van de Kruijs, M. Th. Rekveldt, and H. Fredrikze

Interfaculty Reactor Institute, Delft University of Technology, Department of Neutron scattering and Mössbauer spectroscopy,
Mekelweg 15, 2629 JB Delft, The Netherlands

J. T. Kohlhepp, J. K. Ha, and W. J. M. de Jonge

Eindhoven University of Technology, Department of Applied Physics and COBRA Research Institute,
P.O. BOX 513, 5600MB Eindhoven, The Netherlands

Polarized neutron reflectometry (PNR) has been used to investigate the magnetic interlayer coupling in a MBE-grown Fe/Si/Fe(001) sandwich at room temperature and at 10 K. Both the magnitude and orientation of the magnetic moments of the Fe layers are obtained from a rigorous analysis of the PNR data. Orthogonal configurations of the Fe magnetizations were observed, providing unambiguous evidence for the presence of a biquadratic term in the exchange coupling energy. The competition between the bilinear and biquadratic exchange couplings results in distinct orthogonal and antiparallel configurations of the Fe magnetizations at room temperature. A previously unresolved magnetic configuration in the room-temperature hysteresis curve was identified by the PNR measurements as a 180° spin-flop transition. The dominant role of the biquadratic coupling at low temperatures is evident from the orthogonal configuration of the magnetizations at remanence in the measurements at $T = 10$ K. The magnetic configurations deduced by PNR are in good agreement with those obtained by fitting the magnetic hysteresis loops using a global energy minimum calculation.

I. INTRODUCTION

The interlayer exchange coupling between ferromagnetic layers across nonferromagnetic spacers has been a topic of enormous interest in the past years. Its presence along with the crystalline magnetic anisotropies and external magnetic fields can lead to interesting arrangements of the magnetization directions of the individual layers.[1,2] These arrangements can be experimentally determined using polarized neutron reflectometry (PNR)[3–6] with polarization analysis or, in a somewhat less direct way, by analyzing magnetization loops.[7–10]

The interlayer exchange coupling energy per unit surface area is generally written as $E_{ex} = -J_1\cos(\Delta\theta) - J_2\cos^2(\Delta\theta)$, where J_1 and J_2 are the bilinear and biquadratic coupling coefficients, respectively, and $\Delta\theta$ is the relative angle between the magnetizations of the ferromagnetic layers. Typically, the Heisenberg-like bilinear coupling (J_1) shows an oscillatory dependence on the interlayer thickness. The origin of this oscillatory behavior can be found in the detailed topology of the spacer Fermi surface. The biquadratic coupling contribution (J_2) is recognized to depend strongly on the thickness, composition, and structure of the interlayer. Its origin is attributed to extrinsic factors such as fluctuations in the interlayer thickness[11,12] or superparamagnetic impurities in the spacer layer ("loose spins").[8,13,14] An overview of these mechanisms can be found in Ref. 15.

One system of particular recent interest is that of ferromagnetic Fe layers *nominally* separated by a semiconducting Si layer. The Fe/Si system is well suited for fundamental studies of the antiferromagnetic exchange coupling between two magnetic layers, but it is also interesting because of its application in neutron beam optics.[16] The bilinear and biquadratic interlayer exchange in Fe/Si and their temperature dependence have been intensively studied by several groups and were shown to depend strongly on the properties of the iron silicide that is formed by intermixing at the Fe/Si interfaces during growth.[5,10,17–22] In contrast to the oscillatory nature common in metallic systems, a strong antiferromagnetic coupling ($J_1<0$) was found in MBE-deposited Fe/Si/Fe trilayers, with J_1 exponentially decreasing for increasing spacer thickness.[23] An additional biquadratic contribution to the exchange coupling was also identified by a detailed analysis of magneto-optical Kerr effect (MOKE) measurements. From the distinct temperature and exponential thickness dependence of the derived coupling parameters J_1 and J_2, the exchange coupling was identified to be originated from "loose spins" in the during the deposition formed crystalline iron-silicide spacer layer.[7,8,20]

Although the interlayer exchange in single-crystalline Fe/Si/Fe(001) sandwiches has been determined by a hysteresis loop analysis, no *direct* observation of the microscopic spin orientations was obtained. Furthermore, it was recently recognized that fluctuations of the bilinear coupling due to fluctuations in the interlayer thickness both in-plane and throughout a multilayer stacking may mimic biquadraticlike behavior in the magnetization curves.[6] In the present work, we combine information obtained from PNR, grazing incidence x-ray reflection (GIXR) and MOKE to give a detailed description of the magnetization configurations in exchange coupled Fe/Si/Fe(001). The particular advantage of PNR is that it gives *vectorial* information about the magnetization (both magnitude and orientation) of each layer, and hence the relative angle between the magnetizations can be determined.

The layout of the paper is as follows. Section II describes the sample preparation and the experimental methods used in this work. In Sec. III the structure of the sandwich is determined by GIXR. The magnetic characterization of the sandwich is presented and discussed in Sec. IV, with Sec. IV A focussing on MOKE results and Sec. IV B focussing on PNR experiments. Finally, conclusions are presented in Sec. V.

II. EXPERIMENTAL METHODS

The Fe/Si/Fe sandwich was grown at the Eindhoven University on a Ge(001) substrate in a molecular-beam epitaxy (MBE) system (VG-Semicon V80M) with a base pressure of 2×10^{-11} mbar. Prior to deposition of the layers, the Ge(001) substrate was cleaned by several Ar^+ sputter and anneal treatments until a sharp (2×1)-LEED pattern was observed. The Fe layers were deposited by an *e*-gun source with feedback control of the flux, whereas the Si was evaporated from a temperature-stabilized effusion cell. All nominal layer thicknesses were controlled by calibrated quartz-crystal monitors. After addition of a Si capping layer to avoid oxidation, the final *nominal* composition of the sandwich was as follows: Ge(001)/60 Å Fe/14 Å Si/45 Å Fe/40 Å Si. The nominal Si thickness of 14 Å was chosen to have a well-defined bilinear and biquadratic coupling as found earlier in identical samples.[7,8] More detailed information about the growth dynamics, the structural quality and the Fe/Si interdiffusion can be found in Ref. 20.

In the present study, additional structural information was gained from GIXR data accurately taken at room temperature. A standard $\theta - 2\theta$ reflectometer (Philips X′Pert system) with a wavelength of $\lambda = 1.542$ Å ($CuK_\alpha, E = 8.05$ keV) was used. The reflection angle θ was varied between $\theta = 0.5°$ and $5°$, resulting in a wave vector transfer range of $Q = 4\pi\sin(\theta)/\lambda = 0.07 - 0.7$ Å^{-1}. The slits that define the beam size also determine the angular divergence of $\Delta\theta \approx 0.05°$, resulting in an instrumental resolution of $\Delta Q \approx 3 \times 10^{-3}$ Å^{-1}.

For the magnetic characterization, MOKE and PNR experiments were performed at room temperature and at $T = 10$ K. The longitudinal MOKE hysteresis loops were obtained using an incident laser beam spot size of the order of 0.1 mm. The PNR experiments were carried out at CRISP, the time-of-flight reflectometer at the ISIS spallation source, with an available wavelength range of $\lambda = 2 - 6.5$ Å for polarized neutrons.[24,25] The experimental settings for the fixed glancing angle of incidence and for the size of the beam slits combined to an effective instrumental resolution of $\Delta Q/Q \approx 0.10$. FeCoV/TiN$_x$ super-mirrors and Drabkin spin-flippers were used to define the incident beam polarization and perform the analysis of the reflected beam polarization. Additionally, small guide fields were present along the flight path of the polarized neutron beam to avoid depolarization effects.

III. STRUCTURE CHARACTERIZATION

The x-ray data taken at room temperature are plotted in Fig. 1. Reflectivity calculations using a standard matrix ele-
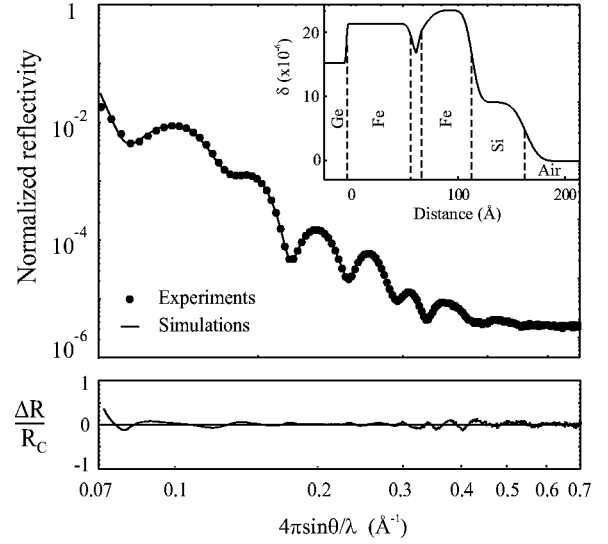

FIG. 1. Normalized specular x-ray reflectivity curve of the Fe/Si/Fe(001) sandwich. Markers are shown for every fifth data point. The inset shows the dispersion parameter δ obtained from fitting the model calculations to the experimental data. The discrepancy between calculated and experimental data is shown at the bottom.

ment formalism[26,27] are fitted to the experimental data. The sandwich is partitioned into four slabs, corresponding to the four deposited layers. The solutions of the electromagnetic wave equation inside the slabs are represented by matrices that depend on the thickness t and the refractive index n of each slab and on the wave vector k inside each slab. The index of refraction n of a material consisting of different elements i is given by

$$n = \sqrt{1 - \frac{r_0\lambda^2}{\pi}\sum_i N_i f_i} \simeq 1 - \frac{r_0\lambda^2}{2\pi}\sum_i N_i f_i, \quad (1)$$

where r_0 is the classical electron radius, and N_i and f_i are the atom number density and scattering factor of each element. The scattering factor consists of a real part representing the coherent scattering of the x rays and an imaginary part representing the absorption of the x rays. Thus Eq. (1) is commonly written as

$$n = 1 - \delta - i\beta, \quad (2)$$

with the dispersion $\delta = \text{Re}[(r_0\lambda^2/2\pi)\Sigma_i N_i f_i]$ and the absorption $\beta = \text{Im}[(r_0\lambda^2/2\pi)\Sigma_i N_i f_i]$.

From the sequence of all layer matrices, the reflectivity of the sample is calculated as a function of the wave vector transfer $Q = 4\pi\sin(\theta)/\lambda$, where θ is the grazing angle of incidence. The effect of interdiffusion between two deposited layers is incorporated by analytical expressions that describe the continuous change in the refractive index between two layers by an error-function profile.[28] The r.m.s. surface roughness parameter σ quantifies the width of the error function. All the calculated spectra were convoluted with the appropriate resolution function.

The fitting parameters in the data analysis are the thickness t, the dispersion δ, and the r.m.s. surface roughness σ for each slab in the model. The absorption parameter β was

TABLE I. The layer thickness t, dispersion δ and r.m.s. surface roughness σ, as refined from the fitting of model calculations to the experimental x-ray reflectivity data. The layer thickness in parentheses is the nominal layer thickness; the dispersion in parentheses is taken from literature (Ref. 29).

Layer	t (Å)	δ ($\times 10^{-6}$)	σ (Å)
Si	48 (40)	9.1 (7.6)	9.5
Fe	46 (45)	23.4 (22.5)	5.6
Si	9 (14)	16.8 (7.6)	9.5
Fe	59 (60)	21.3 (22.5)	3.2
Ge		15.1 (14.5)	0.8

taken from literature[29] because the absorption of x rays in the sandwich does not play an important role in the reflectivity calculations. The discrepancy between the model calculations and the experimental data is quantified by

$$E = \frac{1}{N} \sum_{j=1}^{N} \left(\frac{\Delta R(j)}{R_C(j)} \right)^2, \qquad (3)$$

where $\Delta R(j) = R_C(j) - R_M(j)$ and $R_C(j)$ and $R_M(j)$ are the calculated and measured reflectivities at reflection angle $\theta(j)$. Minimization of Eq. (3) was performed in two separate steps. First, a genetic algorithm (GA) was used to obtain a global minimum of E. Genetic algorithms have the distinct advantage of significantly reducing the chance of hitting a local minimum and have been successfully used to analyze GIXR data in the past.[30,31] Subsequent minimization by a hill-climbing algorithm (HC) refines the parameter values and an absolute minimum of E is reached. The fitted model calculations are shown as a solid line in Fig. 1. In the inset of the figure the depth-profile of the dispersion parameter δ that resulted from the fitting procedure, is depicted. The values of $\Delta R/R_C$ demonstrate that the fit is in excellent agreement with the experimental data over the available experimental wave vector range.

Table I gives the values of the refined model parameters t, δ, and σ. The fitted thicknesses of both Fe layers correspond well with their nominal values and their dispersion values are also close to the bulk value of $\delta_{\text{Fe}} = 22.5 \times 10^{-6}$. The increased thickness of the Si capping layer can be attributed to oxidation of the sample surface. The dispersion value of the Si interlayer clearly differs from that expected for bulk Si ($\delta_{\text{Si}} = 7.6 \times 10^{-6}$). The fitted value of $\delta = 16.8 \times 10^{-6}$ is close to that of FeSi ($\delta_{\text{FeSi}} = 18.3 \times 10^{-6}$), and thus a clear indication of iron-silicide formation in the spacer layer. The reduced value of the fitted apparent interlayer thickness and a σ value as large as the spacer thickness are additional signatures of a *completely* interdiffused, e.g., iron-silicide spacer. A more detailed study of the formation of the iron-silicide interlayers in Fe/Si/Fe(001) using LEED, AES, and Mössbauer spectroscopy was already presented in Ref. 20. But the GIXR data supply additional information: When the reflectivity calculations were fitted to the experimental data under the assumption that the Fe/Si interface width was equal to
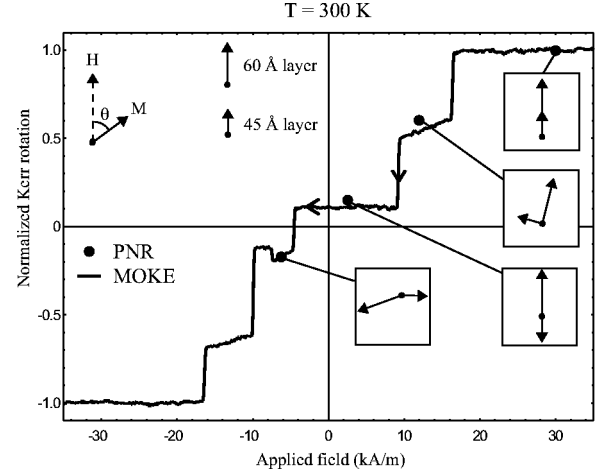

FIG. 2. KERR rotation of the Fe/Si/Fe sandwich at room temperature with the field applied along the [100] easy axis. The round markers indicate data points obtained from PNR experiments. The insets show the magnetic configuration as derived from the polarized neutron reflectivity experiments.

the Si/Fe interface width, the model calculations showed large discrepancies with the experimental data. When separate interface widths were used in the fit, this discrepancy disappeared, resulting in the profile shown in the inset of Fig. 1. Such an asymmetry in the width of the intermixing regions has been previously reported for metal/Si multilayers.[32]

IV. MAGNETIC CHARACTERIZATION

A. MOKE experiments

Figure 2 shows a room-temperature longitudinal MOKE loop with the applied field H along the [100] easy axis. For clarity, only the branch of the down-field sweep is plotted. The magnetization loop can be excellently fitted using global energy minimum calculations of the total relevant magnetic energy which is composed of the cubic magnetocrystalline energy, the Zeeman energy, and bilinear and biquadratic exchange energy contributions.[8] The result of the analysis is the following: As the magnetic field decreases from saturation towards remanence, three distinct regions separated by sudden jumps can be identified. The first plateau where $H > 17$ kA/m corresponds to a saturated magnetic state with parallel orientations of the two layer magnetizations. For 10 kA/m $< H <$ 17 kA/m, the magnetization of the 60 Å layer is oriented parallel to the applied field and the magnetization of the 45 Å layer is oriented perpendicular to it, indicating the presence of a distinct biquadratic contribution to the interlayer coupling. The plateau between $H = -4$ kA/m and $H = 10$ kA/m, which includes the remanent state, is expected to have an antiparallel orientation of the magnetic moments due to the strong bilinear AF coupling. Increasing the negative field, regions with antiparallel, perpendicular and parallel configurations are again identified. An additional magnetic configuration is recognized for -7 kA/m $< H < -4$ kA/m in the MOKE measurement, but
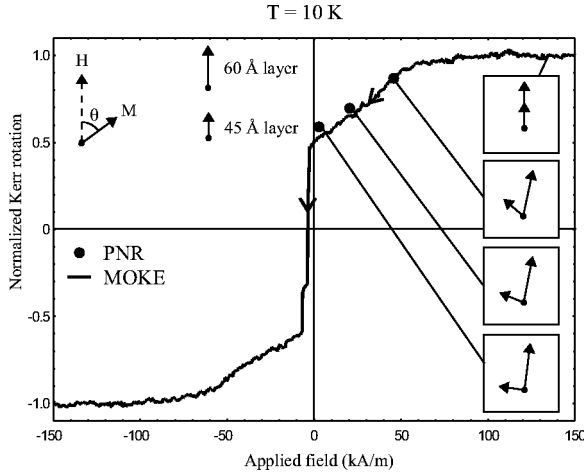
FIG. 3. KERR rotation of the Fe/Si/Fe sandwich at $T = 10$ K with the field applied along the [100] easy axis. PNR experiments were carried out at the marked field values. Magnetic configurations derived from PNR are shown in the insets.
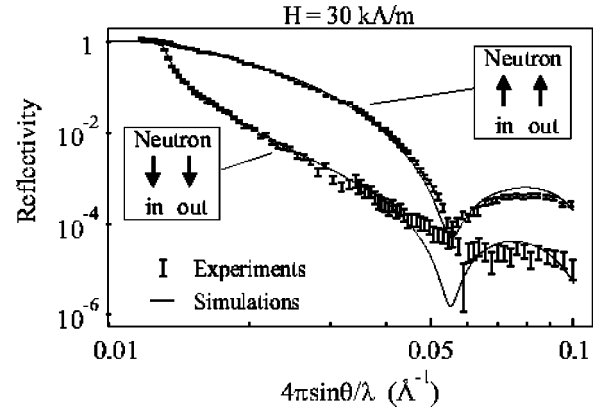

FIG. 4. Room-temperature Fe/Si/Fe(001) reflectivity curves as a function of neutron wave vector transfer at an applied field of 30 kA/m along the easy axis. The inset shows the polarization direction of the incident neutrons (in) and the direction of polarization analysis for the reflected neutrons (out).

its magnetization configurations could not be identified up to now by the simple simulation analysis.

The magnetization behavior at low temperature is quite different from that at room temperature. The down-field magnetization loop of Fe/Si/Fe(001) at $T = 10$ K is shown in Fig. 3. The plateaus observed in the room-temperature hysteresis curve are missing at low temperature. From the analysis of the hysteresis loop by global energy minimum calculations of the total magnetic energy, the magnetization reversal process is found to be a coherent rotation of the magnetic moments and the large remanent magnetization is an indication of 90° alignment of the magnetizations of the ferromagnetic layers at zero applied field.

B. Polarized neutron reflectometry

PNR experiments are carried out to directly confirm the presence of bilinear and biquadratic exchange coupling in the Fe/Si/Fe(001) sandwich and obtain more detailed information about the magnetization reversal processes. PNR with polarization analysis of the reflected beam is unique in its ability to extract a vectorial magnetization profile[33,34] and has been used successfully in studies of the magnetic interlayer coupling in, for instance, Fe/Cr multilayers.[3,35]

At room temperature, first a saturation field of $H = 250$ kA/m was applied along the in-plane [100] easy axis of the Fe/Si/Fe(001) sandwich. Subsequently, the applied field was reduced in steps and PNR "snap shots" were taken at the field values marked in the hysteresis loop of Fig. 2. In all PNR experiments we measured the four detector intensities $I(\uparrow\uparrow)$, $I(\downarrow\downarrow)$, $I(\uparrow\downarrow)$, and $I(\downarrow\uparrow)$, where the first arrow between parentheses marks the direction of the incident beam polarization and the second arrow marks the direction of polarization analysis of the reflected beam. The polarization directions are either parallel ($\uparrow$) or antiparallel ($\downarrow$) with respect to the applied field direction. The detector intensities are normalized to the incident beam intensity and corrected

for the illuminated sample area. Finally, the experimental data were corrected for the efficiencies of the polarizing elements using procedures described elsewhere[36] to obtain the reflectivities $R(\uparrow\uparrow)$, $R(\downarrow\downarrow)$, $R(\uparrow\downarrow)$, and $R(\downarrow\uparrow)$. All data points that were negative or had absolute values smaller than their estimated statistical uncertainties were excluded in the plots.

The reflectivity curves in Fig. 4 were taken at room temperature with an applied field of $H = 30$ kA/m. The ($\uparrow\downarrow$) and ($\downarrow\uparrow$) spin-flipped reflectivities are effectively equal to background levels. The large splitting between the ($\uparrow\uparrow$) and ($\downarrow\downarrow$) non-spin-flipped curves is indicative for a large net magnetization component along the applied field direction. A large net magnetization, together with the absence of any spin-flipped reflectivities, confirms the expectation that the sandwich is saturated with the magnetizations of the 45 Å layer and the 60 Å layer oriented parallel to the applied field direction. For an applied field of $H = 12$ kA/m, high intensity spin-flipped signals are measured (not shown). These spin-flipped intensities are related to components of the magnetization *perpendicular* to the applied field direction and vanish only if such components are not present. Perpendicular components of the magnetizations indicate the presence of a biquadratic contribution to the interlayer coupling. Measurements at $H = 2.5$ kA/m, close to the remanent situation, show only a small splitting between non-spin-flipped reflectivity curves, indicating a small net magnetization. Together with the absence of any spin-flip scattering, this confirms a fully antiferromagnetic configuration, showing the dominance of bilinear coupling at room temperature. The last snapshot was taken at $H = -7.4$ kA/m and the PNR spectra for this field setting are shown in Fig. 5. Again high intensity spin-flipped signals are measured and the Fe magnetizations have components perpendicular to the applied field direction.

The exact magnetic configurations can be obtained by fitting PNR simulations to the experimental data. Analogous to the case of x rays [Eq. (1)], the index of refraction n for neutrons incident on a material consisting of elements i can be written as
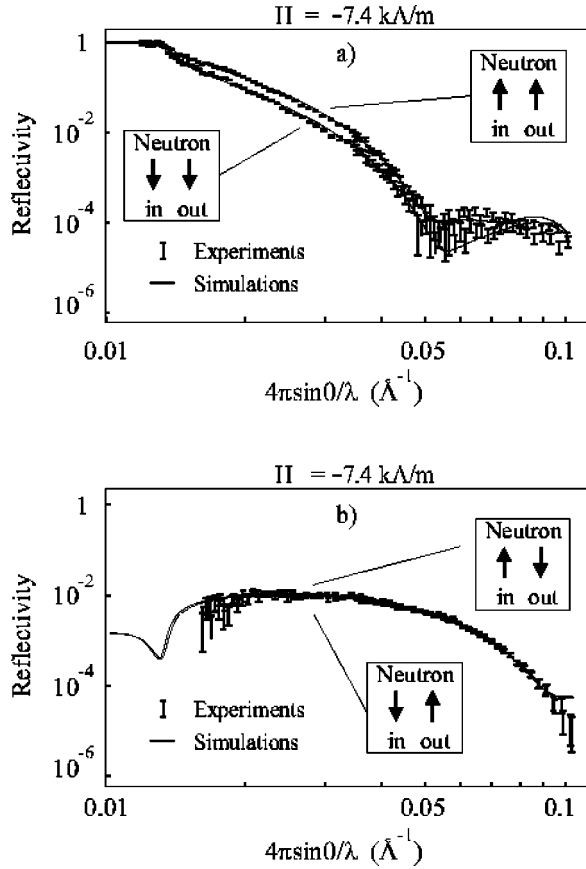
FIG. 5. Non-spin-flipped (a) and spin-flipped (b) reflectivities as a function of wave vector transfer at room temperature with $H = -7.4$ kA/m along the easy axis.

$$n_\pm = \sqrt{1 - \frac{\lambda^2}{\pi} \sum_i N_i(b_i \pm p_i)}, \qquad (4)$$

where b_i is the bound coherent nuclear scattering length and $p_i = C\mu_i$ is the magnetic scattering length, with $C = 0.2695 \times 10^{-4}$ Å/μ_B and μ_i is the net magnetic moment per scatterer in units of Bohr magnetons. $N_i b_i$ and $N_i p_i$ are commonly referred to as the nuclear and magnetic scattering length densities (SLD) of element i. In general, b_i is a complex quantity with a real and imaginary part respectively representing the scattering and the absorption of neutrons. The $\pm$ sign in Eq. (4) refers to the incident polarization of the neutrons, either parallel $(+)$ or antiparallel $(-)$ to the applied field direction.

The nuclear density profile and vector magnetization profile of the Ge(001)/Fe/Si/Fe/Si sample are approximated by a four-slab model, with each slab representing a deposited layer. The solutions of the particle wave equations in these slabs are implemented in a matrix formalism that calculates the spin-dependent neutron reflectivities of magnetically noncollinear media as a function of the neutron wave vector transfer $Q = 4\pi\sin(\theta)/\lambda$.[37] The influence of absorption (imaginary part of b_i) on calculations of the reflectivity is negligible in the wave vector range used in the present PNR

experiments. To our knowledge, no analytical expressions exist that describe the influence of both the nuclear and the magnetic roughness of noncollinear systems on PNR simulations in a similar way as the expressions derived by Névot and Croce for GIXR.[28] To incorporate the effect of interdiffusion at interfaces, additional slabs were added at the interface positions to describe gradual changes in the nuclear density and in the magnetization vector. It turns out that the effect of interdiffusion on the neutron reflectivity calculations is negligible in the experimentally available neutron wave vector transfer range.

The model calculations are fitted to the experimental data by minimization (GA followed by HC) of

$$E = \frac{1}{N} \sum_{j=1}^{N} \left(\frac{\Delta R(j)}{U_R(j)}\right)^2, \qquad (5)$$

where $\Delta R(j)$ is the difference between calculated and measured reflectivity for neutrons of wavelength $\lambda(j)$ and $U_R(j)$ is the statistical uncertainty in the measured reflectivity. The parameters that were refined are the nuclear scattering length density $Nb = \Sigma_i N_i b_i$ in each layer, and the size (M) and orientation (θ) of the magnetization in both Fe layers. The nuclear scattering length density profile at the start of the fitting procedure was obtained from the GIXR results presented in Sec. III. The experimental data at high Q are not of sufficient quality to resolve details in the nuclear and magnetic SLD profiles, making the fit procedure rather insensitive to small changes in the SLD profiles. The number of fitting parameters could be reduced by setting the values of Nb and M to the same value for both Fe layers, without affecting the overall quality of the fit. The fit procedure is much more sensitive to changes in the *orientations* of the Fe magnetizations. Such changes affect the reflectivity over the entire Q range and change the relative contributions of the spin-non-flipped and spin-flipped signals. Model calculations were fitted *simultaneously* to all the room-temperature experimental data by using a common nuclear SLD profile in all model calculations. In this way, the influence of systematical errors in separate data-sets on the fitting procedure is reduced. Furthermore, instead of fitting the spin-asymmetry function that is defined in Ref. 37, we fit model calculations to all four reflectivities $R(\uparrow\uparrow)$, $R(\downarrow\downarrow)$, $R(\uparrow\downarrow)$, and $R(\downarrow\uparrow)$. Fitting all spin-dependent reflectivity curves simultaneously is in general a more sensitive procedure than fitting only the spin asymmetry function.

It was impossible to obtain good fits to the experimental data with a single-domain configuration (i.e., the magnetization M in each Fe layer is that of the magnetization at saturation M_S). A good fit could be obtained only with a systematic reduction of the fitted size of the magnetization at lower fields, with M/M_S dropping to 0.88 at the near-remanent state. This can be explained by the formation of a multidomain state at low fields, where the neutrons coherently probe the averaged magnetization due to their in-plane coherence length of the order of 100 μm. A similar reduction in magnetization at low field was found when PNR experiments on Fe/Cr/Fe sandwiches were analyzed, although the reduction is more pronounced in Fe/Cr/Fe.[4] The stronger reduction re-

TABLE II. The effective magnetization M/M_S and the angles of the 45 and 60 Å layer magnetizations (θ_{45}, θ_{60}) relative to the applied field direction, determined by PNR measurements at room temperature. The normalized Kerr rotation estimated from Eq. (6) has also been listed.

H (kA/m)	θ_{45} (deg.)	θ_{60} (deg.)	$\Delta\theta$ (deg.)	M/M_S	Kerr
30.2	0	0	0	1.0	1.0
12.0	−74	14	88	0.93	0.66
2.5	180	0	180	0.88	0.21
−7.4	92	−110	158	0.89	−0.22

TABLE III. The effective magnetization M/M_S and the angles of the 45 and 60 Å layer magnetizations (θ_{45}, θ_{60}) relative to the applied field direction, determined by PNR measurements at $T = 10\ K$. Also listed is the normalized Kerr rotation estimated from Eq. (6).

H (kA/m)	θ_{45} (deg.)	θ_{60} (deg.)	$\Delta\theta$ (deg.)	M/M_S	Kerr
45.0	−49	12	61	0.94	0.80
20.0	−68	11	79	0.93	0.70
2.5	−82	7	89	0.92	0.63

ported in Fe/Cr/Fe is explained by the fact that the average domain size in the poly-crystalline Fe/Cr/Fe samples is much smaller than in the single-crystalline Fe/Si/Fe samples.

After the introduction of a reduced magnetization of the Fe layers at low applied fields, the fitted model calculations are in good agreement with the experimental data. The fitted values of $Nb = 7.5 \times 10^{-6}$ Å^{-2} for the Fe layers and $Nb = 2.4 \times 10^{-6}$ Å^{-2} for the Si capping layer are in good agreement with those found for Fe and Si in literature:[38] $Nb_{Fe} = 8.1 \times 10^{-6}$ Å^{-2} and $Nb_{Si} = 2.1 \times 10^{-6}$ Å^{-2}. For the interlayer, the fitted value of $Nb = 6.2 \times 10^{-6}$ Å^{-2} was close to that expected for iron silicide $Nb_{FeSi} = 5.6 \times 10^{-6}$ Å^{-2}. Although these PNR results generally confirm the interpretation of the x-ray data, a higher transversal resolution of the nuclear density profile was obtained by GIXR due to the higher maximum momentum transfer and the better overall quality of the x-ray data.

The refined values of the size and the orientations of the Fe magnetizations are given in Table II, with the corresponding magnetic configurations shown in the insets of Fig. 2. The configuration for $H = 12$ kA/m clearly proves the presence of a 90° coupling between both Fe layers. The dominance of the bilinear coupling at room temperature is concluded from the 180° coupling near remanence. An additional magnetic state was recognized in the room-temperature hysteresis loop for -7 kA/m $< H < -4$ kA/m, which configuration could previously not be deduced from analyzing the MOKE data. The PNR results show that this field region corresponds with a spin-flop transition from antiparallel coupled Fe layers oriented parallel to the applied field, to antiparallel coupled Fe layers oriented perpendicular to the applied field.

The room-temperature MOKE signal for a specific magnetic configuration can be estimated from the PNR experiments. The normalized longitudinal Kerr rotation is proportional to the net magnetization component along the applied field direction and may be written as

$$\text{Kerr} = \frac{t_{45}M\cos(\theta_{45}) + t_{60}M\cos(\theta_{60})}{t_{45}M + t_{60}M}, \quad (6)$$

where t_{45} and t_{60} are the Fe layer thicknesses, and θ_{45} and θ_{60} are the respective angles between the magnetization di-

rections of the 45 and 60 Å Fe layers and the applied field direction. The markers in Fig. 2 correspond with the normalized Kerr rotation that is calculated by Eq. (6), using the fitted values of M, t_{45}, t_{60}, θ_{45}, and θ_{60}. Good agreement is found between the predicted and measured normalized Kerr rotation values, confirming the magnetic configurations derived from the PNR experiments.

PNR experiments at low temperature were carried out with the sample mounted in a helium flow cryostat between the poles of an electromagnet. Experiments were performed at applied fields corresponding to the positions marked in the hysteresis loop of Fig. 3. Model calculations were fitted to the experimental data and a good agreement was obtained. The data analysis of the experiments at $T = 10$ K was performed separately from the data analysis of the room temperature experiments to reduce the time needed by the fitting algorithm. A recent simultaneous fit to all data sets at both temperatures does not show any distinguishable differences in the refined model parameters, confirming the absence of systematical errors in the data sets taken at different temperatures.

The refined parameters for the $T = 10$ K measurements are given in Table III. The formation of a multidomain state is again implied by the decrease in the value of M/M_S. The magnetic configurations determined by PNR are shown in the insets of Fig. 3 and indicate a coherent rotation of the magnetizations from parallel alignment at saturation to perpendicular alignment at remanence. The markers in Fig. 3 indicate the Kerr rotation calculated from the PNR results by Eq. (6) and agree well with the results found by MOKE. The presence of a 90° coupling of the Fe layers at remanence confirms the strong increase of the biquadratic coupling with decreasing temperature that was postulated in Ref. 8.

V. CONCLUSIONS

We have systematically studied the magnetization reversal in an exchange coupled Fe/Si/Fe(001) sandwich by combining information from PNR, GIXR, and MOKE. Room-temperature MOKE loops show a distinct steplike behavior that is indicative for the presence of interlayer coupling. In certain field ranges, the PNR results show an orthogonal arrangement of the magnetizations that is due to a significant biquadratic contribution to the total magnetic energy. The antiparallel magnetic alignment at remanence shows that the

dominant coupling at room temperature is bilinear. At $T = 10$ K, the PNR analysis indicates an orthogonal remanent magnetic configuration that becomes parallel at saturation through a coherent rotation of the magnetizations, demonstrating the dominance of the biquadratic coupling at low temperatures.

[1] M. Macciò, M.G. Pini, P. Politi, and A. Rettori, Phys. Rev. B **49**, 3283 (1994).

[2] S.O. Demokritov, J. Phys. D **31**, 925 (1998).

[3] S. Adenwalla, G.P. Felcher, E.E. Fullerton, and S.D. Bader, Phys. Rev. B **53**, 2474 (1996).

[4] J.A.C. Bland, H.T. Leung, S.J. Blundell, V.S. Speriosu, S. Metin, B.A. Gurney, and J. Penfold, J. Appl. Phys. **79**, 6295 (1996).

[5] H. Homma, J.F. Ankner, and C.F. Majkrzak, J. Magn. Magn. Mater. **126**, 257 (1993).

[6] J. Kohlhepp, M. Valkier, A. van der Graaf, and F.J.A. den Broeder, Phys. Rev. B **55**, R696 (1997).

[7] G.J. Strijkers, J.T. Kohlhepp, H.J.M. Swagten, and W.J.M. de Jonge, J. Appl. Phys. **87**, 5452 (2000).

[8] G.J. Strijkers, J.T. Kohlhepp, H.J.M. Swagten, and W.J.M. de Jonge, Phys. Rev. Lett. **84**, 1812 (2000).

[9] C. Chesman, A. Azevedo, S.M. Rezende, F.M. de Aguiar, X. Bian, and S.S.P. Parkin, J. Appl. Phys. **81**, 3791 (1997).

[10] E.E. Fullerton and S.D. Bader, Phys. Rev. B **53**, 5112 (1996).

[11] M. Rührig, R. Schäfer, A. Hubert, R. Mosler, J.A. Wolf, S. Demokritov, and P. Grünberg, Phys. Status Solidi A **125**, 635 (1991).

[12] J.C. Slonczewski, Phys. Rev. Lett. **67**, 3172 (1991).

[13] J.C. Slonczewski, J. Appl. Phys. **73**, 5957 (1993).

[14] M.E. Filipkowski, C.J. Gutierrez, J.J. Krebs, and G.A. Prinz, J. Appl. Phys. **73**, 5963 (1993).

[15] J.C. Slonczewski, J. Magn. Magn. Mater. **150**, 13 (1995).

[16] P. Høghøj, I. Anderson, R. Siebrecht, W. Graf, and K. Ben-Saidane, Physica B **267-268**, 355 (1999).

[17] J.A. Carlisle, A. Chaiken, R.P. Michel, L.J. Terminello, J.J. Jia, T.A. Callcott, and D.L. Ederer, Phys. Rev. B **53**, R8824 (1996).

[18] A.B. Chizhik, K. Fronc, S.L. Gnatchenko, D.N. Merenkov, and R. Zuberek, J. Magn. Magn. Mater. **213**, 19 (2000).

[19] Y. Saito and K. Inomata, J. Phys. Soc. Jpn. **67**, 1138 (1998).

[20] G.J. Strijkers, J.T. Kohlhepp, H.J.M. Swagten, and W.J.M. de Jonge, Phys. Rev. B **60**, 9583 (1999).

[21] J. Dubowik, F. Stobiecki, B. Szymański, Y.V. Kudryavtsev, A. Grabias, and M. Kopcewicz, Acta Phys. Pol. A **97**, 451 (2000).

[22] Y. Endo, O. Kitakami, and Y. Shimada, Phys. Rev. B **59**, 4279 (1999).

[23] J.J. de Vries, J.T. Kohlhepp, F.J.A. den Broeder, R. Coehoorn, R. Jungblut, A. Reinders, and W.J.M. de Jonge, Phys. Rev. Lett. **78**, 3023 (1997).

[24] J. Penfold, R.C. Ward, and W.G. Williams, J. Phys. E **20**, 1411 (1987).

[25] V. Nunez, A.T. Boothroyd, J. Reynolds, J. Penfold, S. Langridge, D.G. Bucknall, P. Böni, D. Clemens, and M.S. Kumar, Physica B **241-243**, 148 (1998).

[26] M. Born and E. Wolf, *Principles of Optics* (Pergamon, London, 1959).

[27] J. Lekner, *Theory of Reflection of Electromagnetic and Particle Waves* (Martinus Nijhoff Publishers, Dordrecht, 1987).

[28] L. Névot and P. Croce, Rev. Phys. Appl. **15**, 761 (1980).

[29] *International Tables for Crystallography*, edited by A. J. C. Wilson (Kluwer Academic, Dordrecht, 1992), Vol. C.

[30] M. Wormington, C. Panaccione, K.M. Matney, and D.K. Bowen, Philos. Trans. R. Soc. London, Ser. A **357**, 2827 (1999).

[31] A. Ulyanenkov, K. Omote, and J. Harada, Physica B **283**, 237 (2000).

[32] E.E. Fullerton, J. Pearson, C.H. Sowers, S.D. Bader, X.Z. Wu, and S.K. Sinha, Phys. Rev. B **48**, 17 432 (1993).

[33] J.F. Ankner and G.P. Felcher, J. Magn. Magn. Mater. **200**, 741 (1999).

[34] C.F. Majkrzak, Physica B **221**, 342 (1996).

[35] J.F. Ankner, H. Kaiser, A. Schreyer, T. Zeidler, H. Zabel, M. Schäfer, and P. Grünberg, J. Appl. Phys. **81**, 3765 (1997).

[36] H. Fredrikze and R.W.E. van de Kruijs, Physica B **297**, 143 (2001).

[37] S.J. Blundell and J.A.C. Bland, Phys. Rev. B **46**, 3391 (1992).

[38] V. F. Sears (unpublished).